Performances of grooved plates falling film absorber

Benoît Michel, Nolwenn Le Pierrès, Benoit Stutz

Performances of grooved plates falling film absorber

Benoit Michel[a], Nolwenn Le-Pierrès[a], Benoit Stutz[a,*]

[a]*LOCIE Laboratory, Universite Savoie Mont Blanc, CNRS UMR5271, Savoie Technolac, 73376 Le Bourget Du Lac, France*

Abstract

This study presents a new plate-type falling film absorber design, consisting in a vertical grooved falling film absorber. The grooves are designed to obtain good absorber plate wettability, even at a low solution flow rate, resulting in a laminar solution flow regime. Using experimental and numerical tools, the vapor absorption on a LiBr falling film solution is characterized for different operating conditions. The impact of absorber length, cooling water inlet temperature, absorber water vapor pressure, solution inlet temperature, LiBr mass fraction and flow rate is investigated. Experimentally, a high absorption rate is achieved: as high as $7{\cdot}10^{-3}$ $\mathrm{kg\,s^{-1}\,m^{-2}}$. Moreover, a 1D stationary model of water vapor absorption in a laminar vertical falling film is introduced and validated. Numerical investigations allow defining the absorber effectiveness for a wide range of operating conditions.

Keywords:
Falling film absorber, Absorption refrigeration, Lithium bromide, Laminar falling film model

Nomenclature

e thickness, m

Cp thermal capacity, $\mathrm{J\,kg^{-1}\,K}$

g acceleration due to gravity, $\mathrm{m\,s^{-2}}$

h specific enthalpy, $\mathrm{J\,kg^{-1}}$

$\tilde{h}_{s,H_2O}$ partial enthalpy of liquid water in LiBr solution, $\mathrm{J\,kg^{-1}}$

l width, m

L_{cap} capillary length, m, m

L_{th} thermal establishment length, m

L_{dif} diffusive establishment length, m

$\dot{m}$ mass flow rate, $\mathrm{kg\,s^{-1}}$

p pressure, Pa

P power, W

Pr Prandtl number,

$\dot{Q}$ heat exchanged with the HTF, W

R thermal resistance, $\mathrm{K\,m^{-2}\,W^{-1}}$

Re Reynolds number,

T temperature, K

ΔT_{cool} subcooling temperature of the HTF, K

*Corresponding author
E-mail: benoit.stutz@univ-savoie.fr (B. Stutz)

x LiBr mass fraction, %wt

Δz discretization height of the exchanger, m

Greek symbols

α convective heat transfer coefficient, $\mathrm{W\,m^{-2}}$

β mass transfer coefficient, $\mathrm{m\,s^{-1}}$

λ thermal conductivity, $\mathrm{W\,m^{-1}\,K^{-1}}$

μ viscosity, $\mathrm{kg\,m^{-1}\,s^{-1}}$

ρ density, $\mathrm{kg\,m^{-3}}$

σ Boltzman constant, $\mathrm{m^2\,kg\,s^{-2}\,K^{-1}}$

Indices/exponent

abs absorbed/absorber

ad adiabatic mode

cd condenser

cool cooling mode

des desorbed/desorber

eq equilibrium

ev evaporator

film film

H_2O liquid water

htf heat transfer fluid

i inlet

iso isothermal mode

int interface

lin linear

max maximum

o outlet

s LiBr solution

v vapor

w wall

1. Introduction

Absorption systems have been used for cooling applications for more than a century. Today, absorption technology emerges in different areas, especially for refrigeration [1], heat pumping [2] or thermal storage [3, 4] applications. In spite of high investment costs and limited efficiency, the increase in the cost of electricity and environmental problems have made this heat-operated cycle more attractive for both residential and industrial applications.
Absorption machines operate with a binary working fluid: a sorbent/sorbate couple. Among the most promising couples for the absorption cycle are the ammonia/water and water/lithium bromide (H_2O/LiBr) combinations [4]. This paper focuses on the H_2O/LiBr working pair, which presents the advantage of being environmentally friendly and does not present a hazard to human health. However, it must be operated at low pressure (a few kPa), making the process performance highly sensitive to leakage [5].
In these machines, the absorber, in which the exothermal absorption phenomenon and coupled heat and mass transfers occur, is one of the main components. It is known to be the least efficient of all the subcomponents of the absorption system, mainly due to the low mass diffusion coefficient of water into the LiBr solution [6]. Moreover, the heat released by the absorption phenomenon at the solution interface leads to an equilibrium condition displacement that limits the phenomenon. Therefore, the absorber is usually the bulkiest and most costly exchanger of the absorption machine. Moreover, its design has a significant impact on the size, cost and performance of system [7].

Among existing absorber technologies, the falling film exchanger is an effective technology for the absorber. It generates a significant exchange surface between the sorbate (water vapor) and the absorbent (LiBr solution) and facilitates the heat transfer from the falling film to the exchanger's cold surface. However, one of the drawbacks of falling film exchangers is the maldistribution of the film on the exchanger surface, which affects flow uniformity at low Reynolds numbers [8]. This well-known phenomenon has encouraged the development of dry patches on the plate and increased the liquid film thickness on the wetted areas [8–10]. The non-wetted areas do not participate in the absorption process, thus decreasing the useful absorber surface and the absorption rate. Heat transfers in wetted areas are also lower compared to the perfect wetted situation, due to the greater thickness of the film.
The comprehension and improvement of the vapor absorption rate into falling film absorber has been the subject of several numerical and experimental studies. The non-wetted areas can be reduced by increasing the flow rate [11], which affects the machine's efficiency [12], by reducing the absorber length or by using chemical and physical surface treatments to increase the absorber surface hydrophilicity and thus its wettability. Furthermore, several absorber falling film configurations have been investigated. The horizontal and vertical tube falling film exchangers are the most commonly implemented and studied [9, 13–17]. However, in order to develop compact absorbers, alternative configurations have been studied, but few studies are available on plate type falling film absorbers. Due to the possibility of accumulating a large number of plates in a small volume, this compact, inexpensive exchanger configuration is attractive, especially for small-capacity absorption machines [13, 18–20]. Furthermore, other studies have examined controlling the thermohydraulic characteristics of the LiBr solution falling film. Promising results were obtained using a hydrophobic membrane to limit the solution film's thickness [6, 21–23]. Another approach consists in macroscopically texturing the absorber plate surface. Mortazavi et al. [7] developed a 3D absorber surface structure integrating fin components in a vertical flat plate. This absorber design provided thin films and uniformly wet absorber surfaces. Thus, absorption rates up to twice as high as on conventional falling film absorbers were obtained.
In this paper, a new plate-type falling film absorber design is presented: a vertical grooved falling film absorber. The grooves are designed to obtain good wettability of the absorber plate, even at low solution flow rates, leading to a laminar solution flow regime. The operation and performance of this absorber are investigated using experimental and numerical tools developed for this purpose. In the first part of this paper, the vapor absorption rate of the exchanger is characterized experimentally for different operating conditions and compared to numerical results. In the second part, its performance is numerically studied for a wide range of operating conditions.

2. Experimental set-up and protocol

2.1. Absorber design

The absorber studied is composed of two welded stainless steel vertical plates within which a heat transfer fluid flows. The plates are 3 mm thick, 100 mm wide. Two absorber

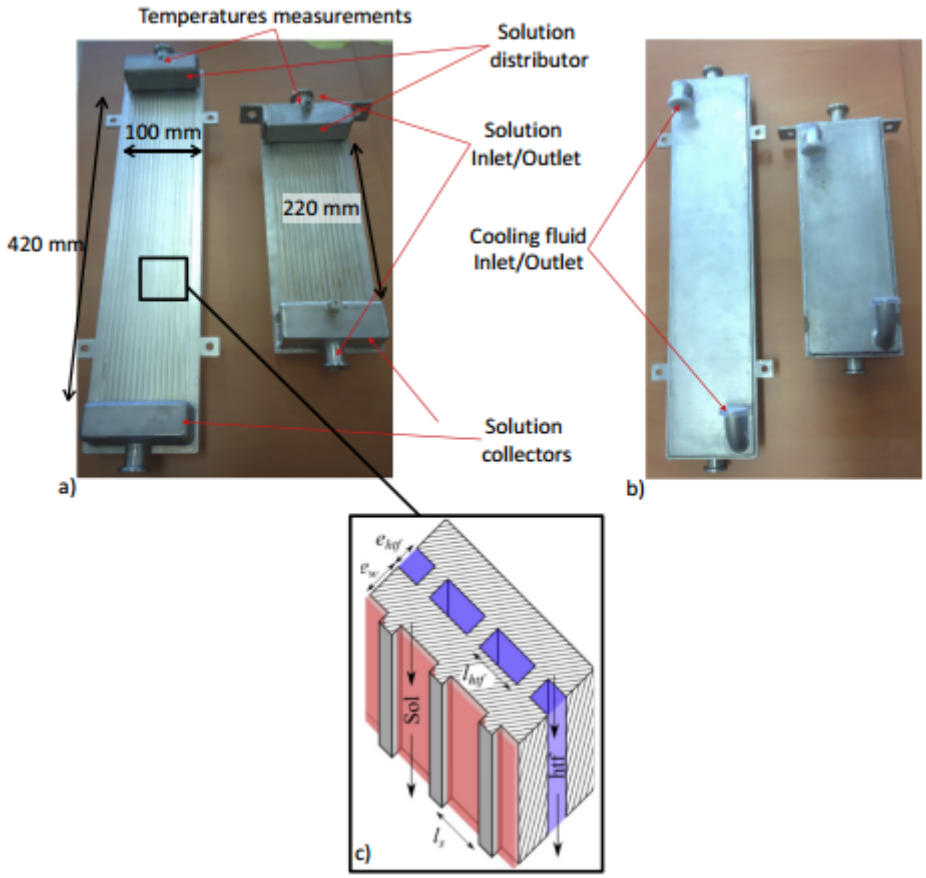

Figure 1: Pictures of the absorbers: a) front view, b) back view. c) Typical section of the exchanger.

lengths (300 mm and 500 mm) are studied in this paper (Figure 1). The solution film flows on the external sides of the plates (considering experimental constraints, the results presented in the present paper were obtained with a single wetted side of the exchanger by the solution). The external surface on which the solution flows is grooved. The vertical grooves are 4 mm wide (ls in Figure 1c) and mm deep. The fins separating the grooves are 2 mm wide. Therefore, the effective wet width of the heat exchangers is 60 mm.
The widths were chosen to ensure the entire wetting of the base of the grooves. Considering the contact angle between the LiBr solution and the stainless-steel plate close to 90 [7] and the capillary length of the LiBr solution in the standard condition of use (x_i = 60 %wt; $T_{s,i}$ = 30 °C; $L_{cap} = \sqrt{\frac{\sigma}{\rho g}} \approx 2.25mm$), the ability of different groove widths to ensure good surface wettability was compared. The width range studied was between 0.5 and 8 mm, and the film Reynolds numbers lower than 400 (laminar flow). Stainless steel is known to be a low wetting substrate for aqueous solutions such as LiBr/H_2O solutions (the contact angle is typically between 80 and 90°). Tests show that when the groove width is lower than the capillary length, gas is entrapped at the wedge of the grooves and liquid is progressively

expelled from the grooves due to a surface tension effect (the solution then preferably flows outside of the grooves). Surface tension effects become negligible when groove width becomes greater than the capillary length, allowing the liquid to wet the base of the grooves. When the grooves are too wide compared to the capillary length ($l_s > 2\ L_{cap}$), the solution never wets the entire base of the grooves for the flow rate range studied. Grooves 4 mm wide ensure satisfactory wetting of the base of the grooves and were therefore chosen for the further design of the absorber. Consequently, grooved plates present the advantage of ensuring significantly greater wetting of the exchange surface compared to flat plate configuration, especially at a low flow rate, as with absorbers. This absorber technology is simple and easy to implement using traditional machining techniques. It is a promising technology for absorption processes. Morover the surface tension effects and the pinning of the triple line of the solution on the side walls of the grooves prevents the formation of wavelets on the film and ensures a laminar flow regime without wavelets on the surface for the entire range of Reynolds numbers studied. The development of wavelets is known to intensify heat and mass transfer along falling films. The stabilization of the free surface flow provided by the grooves can be considered an undesirable effect from the engineering point of view. From the academic point of view, this flow stabilization makes it possible to use standard laminar modeling in good agreement with experiments, because the heat and mass transfer along wavy laminar film is a partially resolved scientific problem.
The LiBr solution is distributed homogeneously within the grooves at the top of the exchanger by a specially designed solution distributor and flows down inside the grooves along the plate (see Figure 1). The solution is collected at the base of the exchanger by a solution collector.
The distributor and collector are 40 mm high. Thus, the effective length of the falling film on the plate is 220 and 420 mm for the 300 and 500 mm long plates, respectively.
Finally, a heat transfer fluid (water) flows in internal rectangular channels (of e_{htf} x l_{htf} = 2 mm x 4 mm) parallel to the exchanger slots. In this study, the LiBr solution and the heat transfer fluid flow in the same direction (downwards). This configuration was selected to obtain a quasi-1D configuration related to heat transfers. This choice moderates the heat transfer coefficients on the heat transfer fluid side in standard exchanger flow configurations (flow regime leading to temperature differences of the heat transfer fluid equal to about 5 °C). These low heat transfer coefficients were compensated in the present study by an increase of the heat transfer fluid flow rate, thus reducing the temperature differences of the heat transfer fluid by about 1 °C. A cross/counter flow configuration is preferred in industrial configurations and will be studied in the future.

2.2. Experimental bench design

An experimental bench was developed to characterize the performance of absorbers dedicated to absorption of water vapor in an LiBr solution. The layout of the experimental set-up is given in Figure 2 and its main features are reported in Table 1.
This experimental bench was designed to ensure stable running conditions for the absorber (solution flow rate, inlet LiBr mass fraction and temperature, working pressure, wall tem-

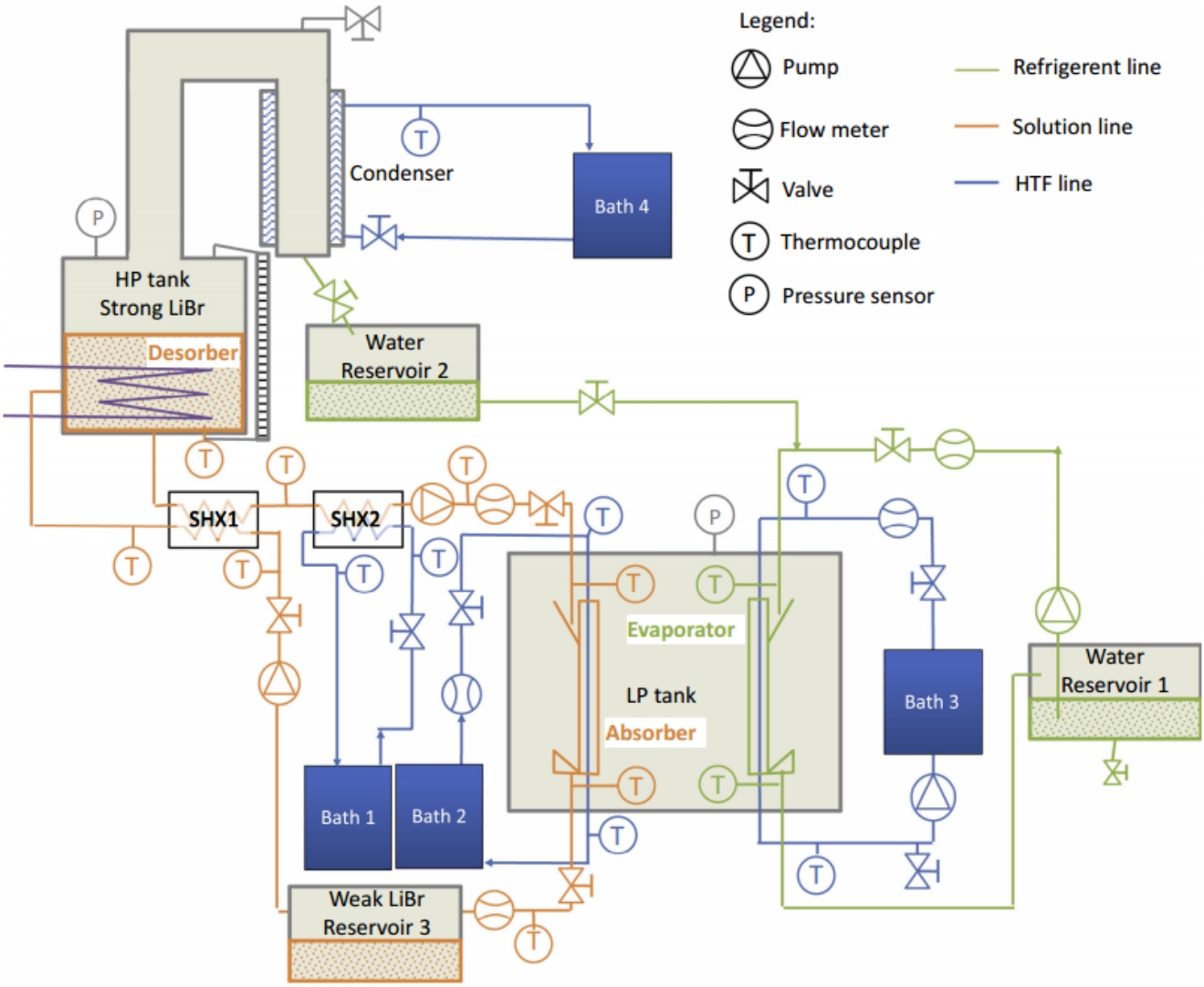

Figure 2: Diagram of the experimental set-up.

perature). It is composed of a LiBr solution line and a refrigerant (water) line. The solution line consists of an absorber placed in the low-pressure tank (LP tank), a desorber (coil exchanger) contained in the high-pressure tank (HP tank), two circulating pumps, two heat exchangers (SHX1 and SHX2) and a solution reservoir (reservoir 3 in Figure 2). The water line consists of an evaporator in the LP tank, a condenser (double envelope tank at high pressure), two water reservoirs (1 and 2 in Figure 2) and a circulating pump.
In the solution line, the strong LiBr solution (i.e., at high mass fraction of LiBr) at high temperature (50-70 °C) exits the HP tank, then is cooled to a controlled temperature by the plate heat exchangers SHX1 and SHX2. In the heat exchanger SHX2, the solution is cooled using a heat transfer fluid (HTF) whose temperature (between 20 °C and 40 °C) is controlled by a thermostatic bath (bath 1). The solution is transferred to the top of the

absorber located in the LP tank, where the absorption phenomenon occurs. The absorber can be cooled by an HTF (water) whose temperature is controlled by a thermostatic bath (bath 2). The weak solution then circulates from the LP tank to a buffer reservoir (reservoir 3). It is then sucked in by a circulating pump and injected into the HP tank, passing through the SHX1 heat exchanger, to be regenerated.
At the same time, water is pumped from reservoir 1 to the top of the falling film evaporator. Evaporation occurs by recovering the heat from a heating circuit whose temperature is controlled by a PID controller using thermostatic bath 3, in order to achieve a constant pressure within the LP tank. The water leaving the evaporator is collected at the base of the evaporator and returns to water reservoir 1. At the same time, the water leaving the condenser is collected and stored in water reservoir 2. Water reservoirs 1 and 2 are separated by a valve.

2.3. Instrumentation and uncertainty measurements

The prototype was strongly instrumented in order to characterize the vertical grooved exchanger performance. The sensor locations are presented in Figure 2. Their characteristics are summarized in Table 2. The measurement points are:

- The density and the mass flow rate of the LiBr solution and the water falling films (solution line and water line) are measured at the inlet and outlet of the absorber and at the inlet of the evaporator, respectively, with Coriolis mass flow meters (OPTIMASS 6400C - KROHNE®). The measurement accuracy (density and the mass flow) is 0.1% of the measured value.

- The flow rates of the HTF circulating through the absorber and the evaporator are measured using two electromagnetic flow meters (OPTIFLUX 1100C - KROHNE®) located at the inlet of each of these heat and mass exchangers. The measurement accuracy is less than 2% of the measured value.

- One pressure sensor (ADIXEN ASD 2002) is located in each of the HP and LP tanks. Their accuracy is 0.5% of the measured value.

- 16 K-type thermocouples measure the LiBr solution and water temperatures at the inlet and outlet of the absorber, desorber, evaporator, heat exchangers SHX1 and 2 and at the inlet of the Coriolis flow meters. The cold junctions are located in an insulated box whose temperature is measured by a high-accuracy PT100 (0.05 °C). Thermocouples were calibrated using a reference probe. Measurement accuracy is estimated to be ±0.15 °C.

Table 1: Maximum capacities of the experimental bench components.

P_{des}	$P_{cool,cd}$ (P_{bath} 4)	P_{ev} (P_{bath} 3)	$P_{cool,abs}$ (P_{bath} 2)	$P_{cool,SHX2}$ (P_{bath} 1)	$\dot{m}_s$	$\dot{m}_{H_2O,ev}$	$\dot{m}_{htf,ev}$	$\dot{m}_{htf,abs}$
2 kW	1.5 kW	2 kW	1.5 kW	1.5 kW	300 kg h^{-1}	200 kg h^{-1}	500 kg h^{-1}	500 kg h^{-1}

Table 2: Range and uncertainty of parameters and sensors.

Measured parameters	Sensor	Studied range	Uncertainty
Temperature	K type thermocouple	5-80 °C	±0.15 °C
Water vapor pressure	ADIXEN ASD 2002	0-100 mbars	±0.5% of the measured value
Solution mass flow rate	Coriolis mass flow meter (OPTIMASS 6400C - KROHNE®)	20-150 $\mathrm{kg\,h^{-1}}$	±0.1% of the measured value
Solution density		1600-1800 $\mathrm{kg\,m^{-3}}$	± 0.1% of the measured value
HTF flow rate	Electromagnetic flow meters (OPTIFLUX 1100C - KROHNE®)	30-80 $\mathrm{L\,h^{-1}}$	±2% of the measured value
Water falling film flow rate	Coriolis mass flow meter (OPTIMASS 1300C - KROHNE®)	80 l/h	±0.1% of the measured value
Calculated parameters	**Calculated from**	**Studied range**	**Uncertainty**
hline Solution mass fraction	T_s and ρ_s	57-60 %wt	$<\pm$ 0.09 %wt
Reynolds number	$\dot{m}_s$	15-350	$<\pm$ 4
Absorption mass flow rate (from enthalpy balance)	$\dot{m}_s$, $T_{s,i}$, $T_{s,o}$, x_i	$4{\cdot}10^{-5}$-$2{\cdot}10^{-4}$ $\mathrm{kg\,s^{-1}}$	$<\pm$ 16% of the measured value

Acquisition was performed using an Agilent 34972 A LXI Data acquisition unit. The acquisition frequency is set at 0.2 Hz. The LiBr physical properties were determined using correlations provided by Ref. [24].
The vapor absorption mass flow rate can be calculated using two methods: based on a mass balance or an enthalpy balance.
The first method uses the absorber inlet solution mass flow rate and inlet and outlet solution mass fractions. The absorption mass flow rate is calculated as:

$$\dot{m}_{abs} = \dot{m}_{s,i}(\frac{x_i}{x_o} - 1) = \dot{m}_{s,o}(1 - \frac{x_o}{x_i}) \tag{1}$$

The accuracy of the absorbed mass measured is given by:

$$\frac{\Delta\dot{m}_{abs}}{\dot{m}_{abs}} = \frac{\Delta\dot{m}_{s,i}}{\dot{m}_{s,i}} + \frac{x_i + x_o}{x_i x_o - x_o}\Delta x \tag{2}$$

with Δx and $\Delta m_{s,i}$ the uncertainty on the mass fraction and the mass flow rate measurements, respectively (see Table 2).
For a low mass fraction difference between the inlet and outlet of the exchanger, the mass flow rate term uncertainty ($\Delta\dot{m}_{s,i} \approx 0.1\%$) is negligible compared to the mass fraction term uncertainty ($\Delta x \approx 35\%$) and the accuracy can be evaluated as:

$$\frac{\Delta\dot{m}_{abs}}{\dot{m}_{abs}} = \frac{2\Delta x}{(x_i - x_o)} \tag{3}$$

For example, for a mass fraction difference of 0.005%wt, the absorbed mass uncertainty is estimated as 36% of the calculated value.
In this study, the small absorber lengths do not allow obtaining significant mass fraction differences (0.005-0.7%wt), so the absorption rate cannot be calculated accurately with this mass balance method.
A second method, based on an enthalpy balance on the LiBr solution, calculates the absorption mass flow rate. These calculations were detailed and compared by Flores [25]. In this method, the outlet solution mass fraction and flow rate measurements are not used and the

outlet enthalpy is estimated from a first-order Taylor expansion:

$$h_{s,o} = h_{s,x_i,T_{s,o}} + \left.\frac{\partial h}{\partial x}\right|_{x_i,T_{s,o}} (x_o - x_i) \tag{4}$$

with $h_{s,i}$ the inlet solution enthalpy, $h_{s,x_i,T_{s,o}}$ the solution enthalpy at the inlet mass fraction and outlet temperature and $\left.\frac{\partial h}{\partial x}\right|_{x_i,T_{s,o}}$ the derivative of the enthalpy as a function of the mass fraction, at the inlet mass fraction and outlet temperature. The enthalpies and these derivatives are determined from the solution temperature and concentration measurements and using correlations provided by Ref. [24].
From the total mass balance:

$$\dot{m}_{s,i} = \dot{m}_{s,o} - \dot{m}_{abs} \tag{5}$$

and the salt mass balance:

$$x_i = \frac{\dot{m}_{s,o}}{\dot{m}_{s,i}} x_o \tag{6}$$

we can write:

$$x_i - x_o = \frac{\dot{m}_{abs}}{\dot{m}_{s,i} + \dot{m}_{abs}} x_i \tag{7}$$

Therefore, the energy balance is:

$$\begin{aligned} \dot{m}_{s,o} h_{s,o} &= \dot{m}_{s,i} h_{s,i} + \dot{m}_{abs} \Delta h_{lv} + \dot{Q}_{htf} \Leftrightarrow \\ \dot{m}_{s,o} \left(h_{s,x_i,T_{s,o}} - \frac{\dot{m}_{abs}}{\dot{m}_{s,i} - \dot{m}_{abs}} x_i \left.\frac{\partial h}{\partial x}\right|_{x_i,T_{s,o}} \right) &= \dot{m}_{s,i} h_{s,i} + \dot{m}_{abs} \Delta h_{lv} + \dot{Q}_{htf} \end{aligned} \tag{8}$$

with $\dot{Q}_{htf}$ the heat exchanged with the HTF (in adiabatic conditions, $\dot{Q}_{htf} = 0$ W ; in cooled conditions, $\dot{Q}_{htf} < 0$ W.
Finally, an analytical solution of the absorption rate is obtained:

$$\dot{m}_{abs} = \frac{\dot{m}_{s,i}(h_{s,i} - h_{s,x_i,T_{s,o}}) + \dot{Q}_{htf}}{x_i \left.\frac{\partial h}{\partial x}\right|_{x_i,T_{s,o}} - h_{s,x_i,T_{s,o}} - \Delta h_{lv}} \tag{9}$$

The uncertainty values of the calculated parameters are summarized in Table 2. Using the methodology suggested by Moffat et al. [26], function uncertainty is calculated numerically using the uncertainty contribution of each variable of the function measured. The accuracy of the absorption mass flow rate calculated using the enthalpy balance is then evaluated at 11% for the experiment, with a mass fraction difference of 0.005%wt, and to be less than 16% of the calculated value, for all the operating conditions studied in this paper. Therefore, in this paper, only the absorption mass flow rate calculated with the enthalpy balance method is used.

2.4. Experimental protocol

Two vertical grooved absorbers (220 mm and 420 mm long) were characterized. The absorption flow rate of these absorbers was determined for different experimental conditions: two operating modes (adiabatic and cooled, with various absorber cooling intensity levels), various solution flow rates, and various temperatures and mass fraction conditions.
In adiabatic mode, the heat transfer fluid flow rate is set at zero. The absorbing falling film does not exchange any heat with the exchanger plate. The heat generated by absorption is then entirely used to heat the solution film. However, the absorption is still possible given the inlet solution equilibrium deviation with the vapor (the solution inlet temperature is lower than the equilibrium temperature at the reactor vapor pressure). In the cooled mode, the HTF flow cools the absorber. The HTF flow is not sufficient to ensure a uniform temperature of the plate. In the isothermal case, the HTF flow rate is high enough to ensure an HTF temperature difference less than 0.2 °C and therefore the temperature of the plate is uniform.
In the following, the Reynolds number of the falling film is defined as:

$$Re = \frac{4\dot{m}_{s,i}}{\mu_i l_s} \tag{10}$$

with l_s the effective width (wet width) of the absorber.
The Reynolds number is determined using inlet conditions (mass flow rate temperature and mass fraction of the LiBr solution). In the Reynolds number range tested (15-350) the solution flow is laminar.
The experimental conditions tested are summarized in Table 3. These conditions correspond to standard operating conditions of the absorption machine [9, 12, 27]. The results presented in the following sections are averaged values over 15 min of recorded data when the steady state is reached. The system is considered to have reached the steady state when the variation of the absorbed water mass flow (calculated using eq. (4)) is less than $5 \cdot 10^{-6}$ kg s^{-1} (around 5% of the total absorbed water mass flow) over a minimum duration of 15 min.
Furthermore, in order to limit the presence of noncondensable gases and although the air leaks are low in this experiment (around 0.2 Pa h^{-1} for the LP tank when the pressure is 20 mbar, and around 1 Pa h^{-1} for the HP tank when the pressure is 5 mbar), the noncondensable gases were expelled before each experiment using a vacuum pump. The vacuum pump did not run during the experiments so that it would have no impact on the mass balances calculated between the evaporator and the absorber.

3. Absorber model

3.1. Model description

A 1D stationary model was developed at the LOCIE laboratory to describe water vapor absorption on a vertical falling film exchanger. The exchanger modeled is composed of a metal plate, where the LiBr solution flows, placed in a saturated water vapor vessel,

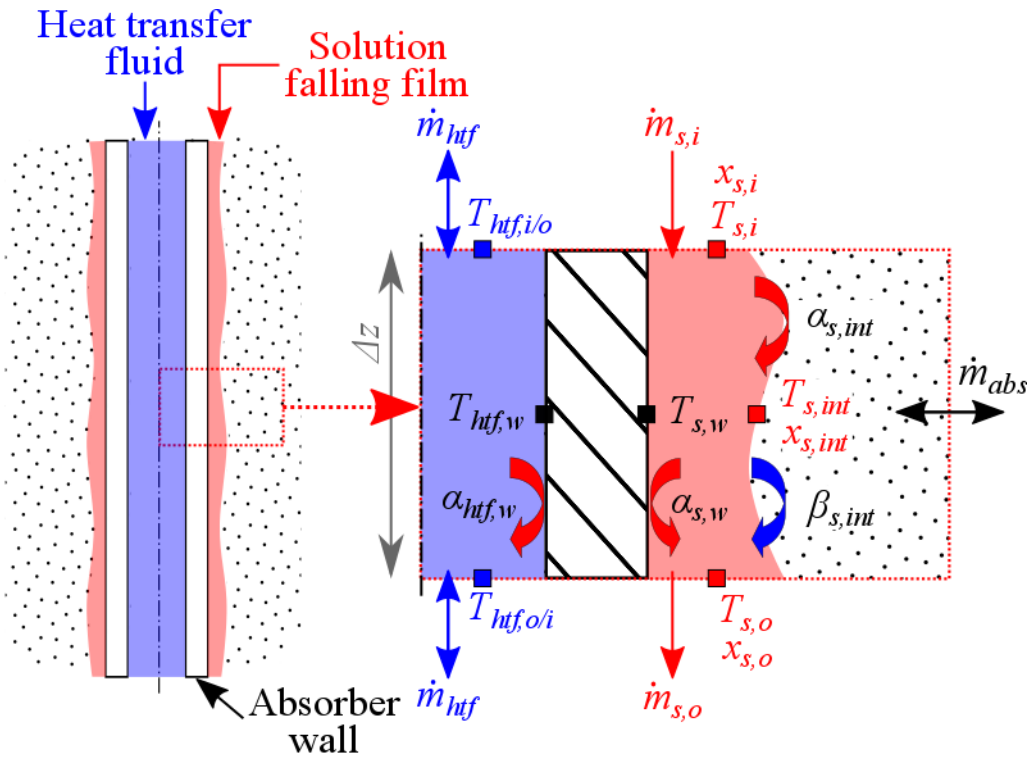

Figure 3: Diagram of the vertical falling film absorber.

permitting the interaction between the vapor and the LiBr solution. The absorber plate is cooled by a heat transfer fluid circulating inside the metal plate (see Figure 3).
This model has already been described in detail in previous papers [28]; therefore, only the main hypotheses and equations are presented here. The modeling approach consists in a nodal division along the solution falling film, the solution vapor interface, the metal plate and the heat transfer fluid. For the absorbers described in section 2.1, the absorber is discretized into 400 identical elements. The energy balance on these elements as well as mass and species balance for the falling film solution are solved under stationary conditions. The model was implemented using the Octave® software.
Additional simplifying assumptions are used:

- The solution flow is laminar. The development of boundary layers at the vapor/solution and wall/solution interfaces is considered and depends on the variation of the heat and mass convection coefficients along the absorber.
- The solution at the vapor/solution interface is considered at equilibrium with the vapor phase.
- The heat conduction along the vertical absorber plate is ignored.
- The heat and mass exchanged between the phases for each element are calculated

with the average temperatures and mass fractions of each phase ($\bar{T} = \frac{T_i + T_o}{2}$) and ($\bar{x} = \frac{x_i + x_o}{2}$).

- The variations of the kinetic and potential energies of the fluids are ignored.
- Lithium bromide salt has a very low vapor pressure and is assumed in this analysis to be nonvolatile [29]. Moreover, it is considered that there is no noncondensable gas in the absorber vessel. The gas in the system is therefore assumed to be pure water vapor
- The vapor pressure is considered homogenous
- There are no heat exchanges with the environment.

Table 3: Experimental conditions tested.

	Solution inlet temperature, $T_{s,i}$ (°C)	Solution Reynolds number	Absorber HTF flow rate ($L\,h^{-1}$)	Solution inlet mass fraction, x_i (%wt)	Evaporator HTF flow rate ($L\,h^{-1}$)	Water falling film flow ($kg\,h^{-1}$)	Vapor pressure, p_v (Pa)	Plate length (mm)
Range	20-40	15-350 ($\dot{m}_{s,i}$ = 20 -150 $kg\,h^{-1}$)	0 (adiabatic) or 30-60 (cooled)	57-60	**30**	**15**	**1000**	**220-420**
Nominal conditions	**30**	**100**	**0**	**60**				**220**

From these assumptions, the mass, energy and species balance on the different elements are written as follows:

- Mass, species and energy balance of the solution film:

$$\dot{m}_{s,i} - \dot{m}_{s,o} + \dot{m}_{abs} = 0 \tag{11}$$

$$\dot{m}_{s,i} x_i - \dot{m}_{s,o} x_o = 0 \tag{12}$$

$$\dot{m}_{s,i} h_{s,i} - \dot{m}_{s,o} h_{s,o} + \dot{m}_{abs} h_v + \alpha_{s,w} l_{s,w} \Delta z (T_{s,w} - \bar{T}_s) = 0 \tag{13}$$

- Mass and energy balance at the interface between the vapor and the solution film:

$$\dot{m}_{abs} - \beta_{s,int} \rho_{H_2O} l_{s,int} \Delta z (\bar{x} - x_{int}) = 0 \tag{14}$$

$$\dot{m}_{abs} \left(h_v - \tilde{h}_{s,H_2O} \right) - \alpha_{s,int} l_{s,int} \Delta z (T_{s,int} - \bar{T}_s) = 0 \tag{15}$$

with x_{int} the equilibrium condition at the interface between the vapor and the solution film:

$$x_{int} = x(p_v, T_{s,int}) \tag{16}$$

- Energy balance of the heat transfer fluid:

$$\dot{m}_{htf}\left(h_{htf,i} - h_{htf,o}\right) - \alpha_{htf,w} l_{htf,w} \Delta z (T_{htf,w} - \bar{T}_{htf}) = 0 \tag{17}$$

- Energy balance at the interface between the solution film and the absorber wall:

$$\alpha_{s,w} l_{s,w} \Delta z (\bar{T}_s - T_{s,w}) + \frac{\lambda_w}{e_w} \Delta z l_{s,w} \left(\bar{T}_{htf,s} - T_{s,w}\right) = 0 \tag{18}$$

- Energy balance at the interface between the heat transfer fluid and the absorber wall:

$$\alpha_{s,htf} l_{s,htf} \Delta z (\bar{T}_{htf} - T_{s,htf}) + \frac{\lambda_w}{e_w} \Delta z l_{s,w} \left(T_{htf,w} - \bar{T}_{htf,s}\right) = 0 \tag{19}$$

The convective heat and mass transfer coefficients at the solu tion film interfaces ($\alpha_{s,w}, \alpha_{s,int}$ and $\beta_{s,int}$) are calculated using the correlations obtained by Brauner for a laminar LiBr solution film flowing over a constant temperature plate surface [30, 31]. The calculation of these coefficients requires the determination of the solution film thickness. This is calculated using the equation developed by Carey [32] for a laminar film considering a parabolic velocity profile. The convective heat transfer coefficient between the heat transfer fluid and the absorber plate ($\alpha_{htf,w}$) is calculated by the classical Dittus-Boelter equation for an internal flow when the flow is turbulent [33] and with the correlations described in Refs. [20, 33] when the flow is laminar. No transitional flow for the heat transfer fluid is considered in this model: the flow evolves from laminar directly to turbulent (and inversely) at a fixed Reynolds number of 4000.

3.2. Absorption simulation

The changes in the temperature and mass fraction of the solution along the 420-mm absorber plate for nominal conditions ($T_{s,i}$ = 30 °C; Re = 100; x_i = 60 %wt; p_v = 1000 Pa) are given in Figure 4 for two operating modes: isothermal (the absorber plate is cooled at a constant temperature) and adiabatic (no cooling of the absorber plate).
Figure 4a and b shows that the absorption phenomenon leads to a sudden temperature increase at the interface in both adiabatic and isothermal conditions (from 30 °C to 43 °C) from the solution film entrance (z ≈ 0).
In isothermal mode, the temperature of the interface Ts,int reaches a maximum at z = 13 cm before decreasing slowly. The difference between the interface temperature and the average temperature $\bar{T}_s$ of the film decreases in the upstream part of the plate and remains quasi-constant downstream. This can be explained by the entry length (the length for which the thermal boundary layer that develops from the interface reaches the plate: around 4 cm in

this case, see Figure 9) effect, which leads to a high heat transfer coefficient at the entrance. Since the interface is at equilibrium with the vapor phase, the LiBr mass fraction at the interface is directly related to its temperature, as can be seen in Figure 4: the interface mass fraction evolves with the interface temperature. The LiBr average mass fraction $\bar{x}_s$ decreases continuously along the plate due to absorption, and the LiBr mass fraction difference between the bulk liquid and the interface ($\bar{x} - x_{int}$) is only slightly affected by the distance z downstream of the thermal entry length. Temperature and mass fraction changes along the plate in the adiabatic mode are similar to the change in the isothermal mode in the first few centimeters on the plate (in the entry length) and differ downstream. The interface and the bulk temperatures increase continuously along the plate, with the film only heated at its interface by the continuous exothermal absorption of vapor. The difference between the temperature of the interface and the average film temperature continuously decreases along the film and becomes negligible at the end of the plate. The stabilization trend of the film temperature shows the end of the absorption process. The mass fraction difference between the interface and the bulk liquid also decreases continuously along the plate but remains considerable at the end of the plate, the mass diffusion coefficient being significantly smaller compared to the thermal diffusion coefficient.
The cooling effect of absorption machines is directly related to the amount of water absorbed by the solution film at the absorber. Using the model presented, the amount of vapor absorbed by the solution per unit of wetted width in nominal conditions for the adiabatic and isothermal modes are 5.37 $\mathrm{kg\,h^{-1}\,m^{-1}}$ and 6.93 $\mathrm{kg\,h^{-1}\,m^{-1}}$, respectively, for a 220-mm-long absorber and 6.2 $\mathrm{kg\,h^{-1}\,m^{-1}}$ and 9.9 $\mathrm{kg\,h^{-1}\,m^{-1}}$ for a 420-mm-long absorber. The amount of vapor absorbed by the solution determined by the ex- periments will be compared to simulations below.

3.3. Model validation

The 1D model of water absorption in a laminar falling film was compared to experimental results for a wide range of operating conditions obtained by the test bench presented in section 2. The solution mass flow rate (Reynolds number), inlet temperature, inlet solution mass fraction and subcooling effect (the absorber is cooled by a heat transfer fluid whose subcooling temperature difference is ($\Delta T_{cool} = T_{s,i} - T_{htf,i}$) were investigated (Figure 5). Experimental results are presented in the annex and will be discussed further in section 4. For a Reynolds number higher than 50, the model slightly overestimated the absorbed mass by a mean 8.7% (maximum 22%) for the 220-mm plate and 3.6% (maximum 10%) for the 420-mm plate. For Reynolds numbers lower than 50, higher deviations between experimental and numerical results are observed. Indeed, in this case, the model overestimates the mean 36% absorbed mass, with a 69% maximum. This is mainly due to the low wetting of the absorber plate observed experimentally [9] for very low flow rates, resulting in dry regions on the absorber that do not participate in the absorption phenomenon. This difficult wetting phenomenon has already been observed in other experiments and is not considered by the model [7, 9, 10]. Another explanation could be the presence of noncondensable gases in the LP tank, which strongly affects the absorption phenomenon even in a very low proportion.

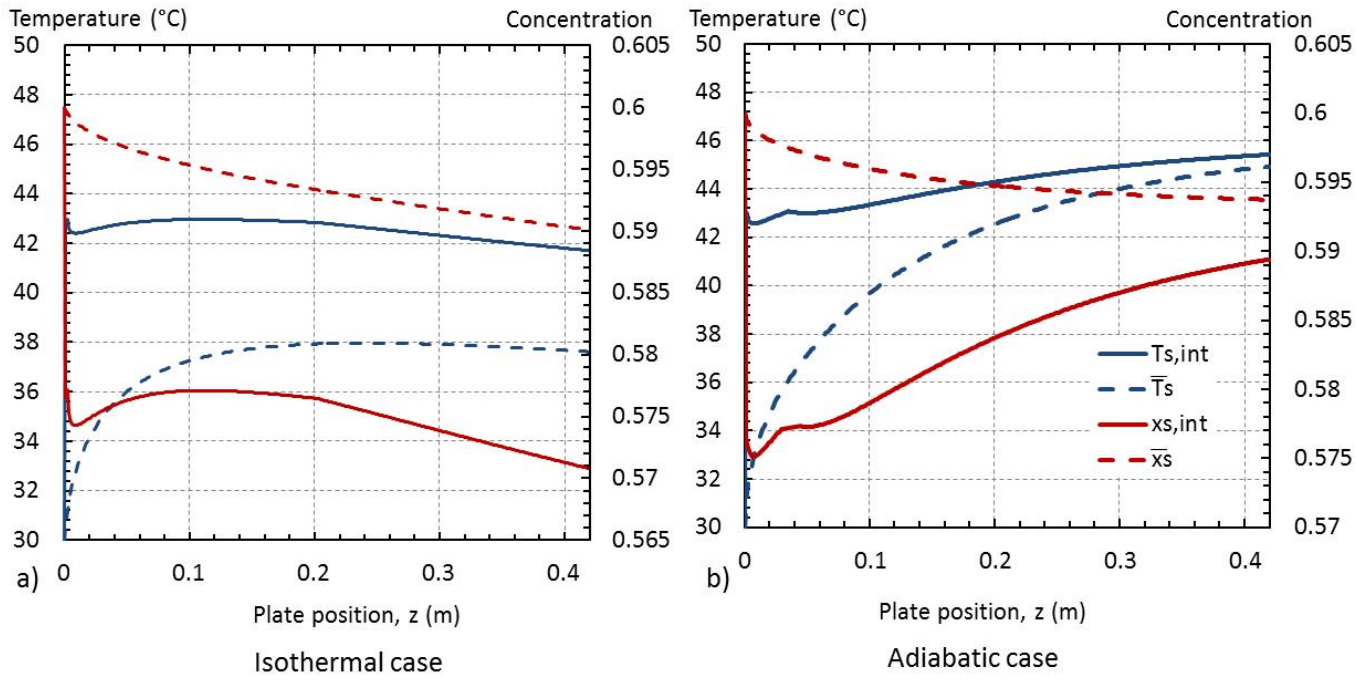

Figure 4: Temperature and mass fraction as they evolve along the solution film for: a) the adiabatic condition and b) the isothermal condition.

4. Absorber performance

This section presents an investigation of the vertical grooved falling film absorber performance, for laminar regimes and for different operating conditions (temperature, mass fraction, flow rate, etc.). In an absorber dedicated to cooling machines, the heat exchanged at the evaporator is directly proportional to the vapor absorbed by the absorber. Therefore, absorber performance is studied using experimental and numerical tools and quantified through the mass of vapor absorbed by the solution falling film (i.e., absorption rate). All the experimental results presented in this section are detailed in the annex.

4.1. Influence of the falling film mass flow rate

The influence of the solution mass flow rate on the absorber performance was evaluated for inlet Reynolds numbers of the solution falling film (eq. (5)) ranging from 15 to 350; the other parameters (pressure, inlet solution temperature, concentration, etc.) were maintained at the nominal conditions described in Table 3. Figure 6 presents experimental and numerical absorption rates for the adiabatic operating mode of 20-mm- and 420-mm-long absorber plates (see section 2.1). Figure 7a shows the influence of the Reynolds number on the absorption rate in the cooled configuration.

The solution flow rate strongly influences the absorption rate. For both absorber lengths

studied, the absorption rate increases approximately three times when the Reynolds number increases from 50 to 300. The flow rate increase makes renewing the solution in contact with the vapor faster and therefore favors absorption. The thickening of the liquid film (caused by the flow rate increase) increases the thermal inertia of the solution. This effect increases the absorption capacity of adiabatic falling films. On the other hand, it increases the thermal resistance between the interface and the plate and thus reduces the cooling capacities of the absorber.

As observed in previous studies [7, 34], the increase of the absorption rate is almost linear at a low flow rate (Re $<$ 100) and slows down at higher flow rates.
As can be deduced from Figure 4, the surface absorption rate decreases with the distance from the top of the plate. The surface absorption rate drops to zero when the bulk liquid film is at equilibrium with the vapor. The plate length needed by a solution film in nominal adiabatic conditions (Re = 100; p_v = 1000 Pa; x_i = 60% wt; $T_{s,i}$ = 30 °C) to reach equilibrium with vapor is about 0.5 m. Therefore, the absorption rate of films flowing over 0.5-m-long adiabatic absorbers varies linearly with the solution mass flow rates for Re $<$ 100 (the solution being at equilibrium with the vapor at the end of the plate). For higher

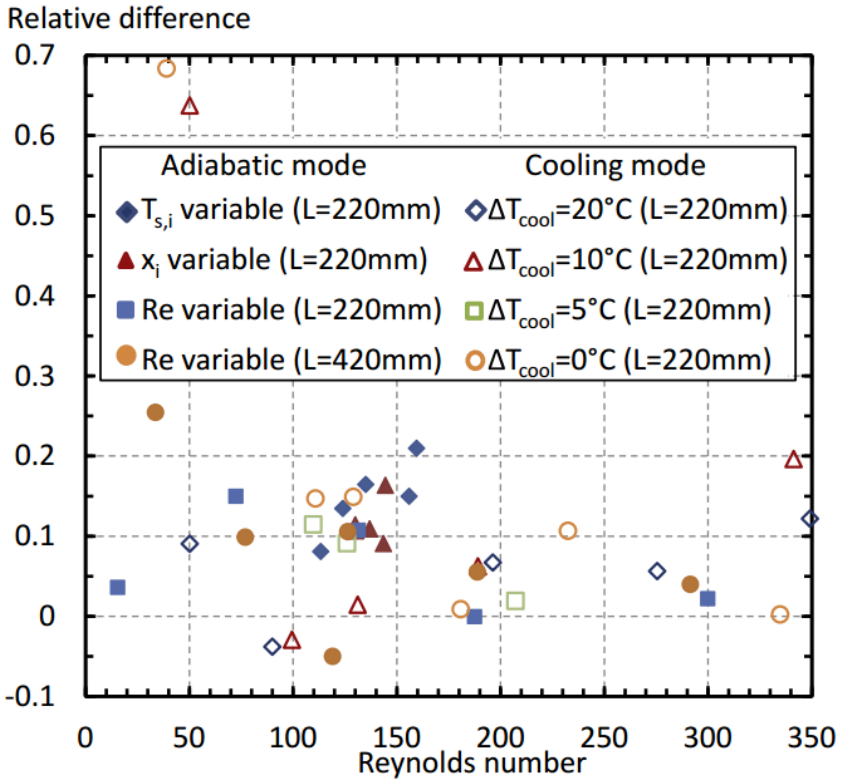

Figure 5: Relative difference between the experimental and simulated results of the absorption rate. A positive relative difference corresponds to a simulated absorption rate greater than the experimental absorption rate.

solution mass flow rates, the absorption rates decrease, and the deviation from equilibrium of the solution with vapor at the end of the plate increases with the solution flow rate. The maximum vapor flow rate that can be absorbed by the solution in adiabatic conditions ($\dot{m}_{abs-ad}^{max}$, corresponding to the vapor flow rate absorbed by an infinitely long absorber) can be calculated by solving a set of five equations:

$$\dot{m}_{s,i} - \dot{m}_{s,o} + \dot{m}_{abs} = 0 \tag{20}$$

$$\dot{m}_{s,i} x_i - \dot{m}_{s,o} x_o = 0 \tag{21}$$

$$\dot{m}_{s,i} h_{s,i} - \dot{m}_{s,o} h_{s,o} + \dot{m}_{abs} h_v = 0 \tag{22}$$

$$T_{s,o-ad} = f(h_{s,o}, x_o) \tag{23}$$

$$T_{s,o-ad} = T_{eq}(p_v, x_o) \tag{24}$$

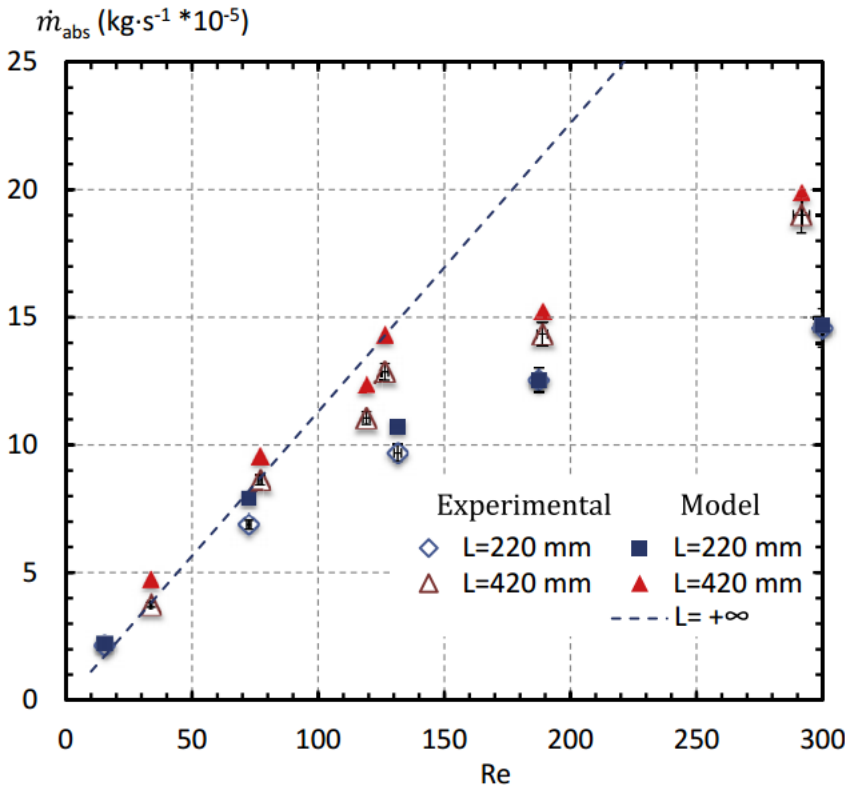

Figure 6: Experimental and numerical absorption rates as a function of the solution Reynolds number, for two absorber lengths in the adiabatic condition.

$\dot{m}_{abs-ad}^{max}$ as a function of the inlet Reynolds number is plotted with a dotted line in Figure 6. The distance between the dotted line and the experimental points shows the degree of deviation from equilibrium of the outlet solution. In other words, when experimental points are located on the dotted line, the solution is at equilibrium with the vapor at the end of the plate. If not, the bulk solution has not reached the equilibrium at the end of the plate. The maximum Reynolds numbers for which the solution in nominal adiabatic conditions reaches equilibrium with vapor at the end of the 220-mm- and 420-mm-long plates can be estimated using Figure 6, and are respectively close to 70 and 120.

4.2. Cooling effect

The cooling effect of the absorber plate is studied in this section. In this case, an HTF flow, whose inlet temperature is controlled, circulates inside the absorber wall (see section 2.4) and cools the LiBr solution falling film. The other parameters, except the solution flow rate, are kept constant at the nominal conditions listed in Table 3.

4.2.1. Cooling effect on the maximum absorption rate

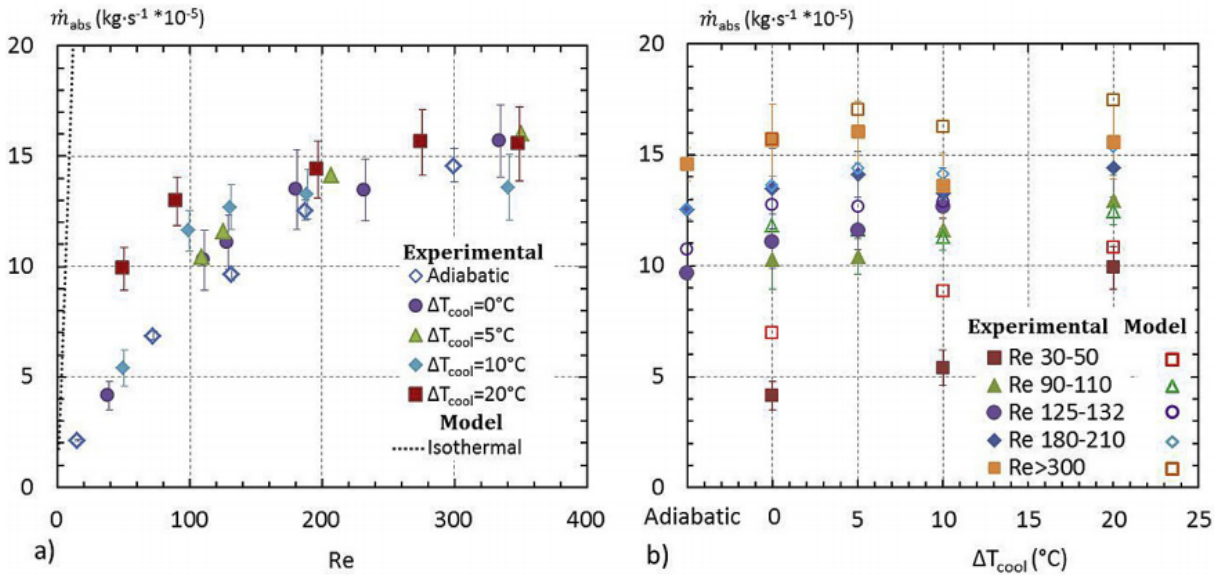

Figure 7: a) Absorption rate as a function of the solution Reynolds number and for different heat transfer fluid inlet temperatures. b) Absorption rate as a function of the heat transfer fluid inlet temperature and for different solution inlet Reynolds numbers. Absorber length: 220 mm.

Contrary to the adiabatic mode, the warming of the solution is not the main parameter that governs heat and mass transfer. Heat transfer coefficients between the film and the heat transfer fluid as well as the mass transfer coefficient between the interface and the bulk liquid film have a greater influence on the absorption rate. The length of the plate needed by a solution film in cooled conditions to reach equilibrium with vapor is significantly higher (a few meters) than in adiabatic mode. Contrary to the adiabatic case, the solution is never

at equilibrium with vapor at the end of the exchangers studied. However, the degree of deviation from equilibrium of the solution with the vapor is substantial and leads to larger mass transfer compared to the adiabatic case.
The maximum vapor flow rate that can be absorbed by the solution film in cooling mode can be calculated for an infinitely long counter-courant absorber, for which heat transfer begins downstream of an initial adiabatic absorption zone. The highest temperature that can be reached by the solution is that obtained at the end of the adiabatic zone when complete absorption is reached. This temperature can be reached by the heat transfer fluid if the fluid that imposes its temperature at the end of the absorber (solution outlet) is the solution (if the limiting fluid is the HTF). The maximum temperature value can be calculated using equations (20)-(24). The heat flux transfer to the HTF is given by equation (25):

$$\dot{Q}_{htf-1} = \dot{m}_{htf} Cp_{htf} \left(T_{s,o-ad} - T_{htf,i}\right) \tag{25}$$

The minimum temperature that can be reached by the solution is the HTF temperature if the limiting fluid is the solution (if the fluid that imposes its temperature at the end of the absorber is the HTF). The heat flux transfer to the heat transfer fluid is given by equation (26):

$$\dot{Q}_{htf-2} = \dot{m}_{s,i} h_{s,i} + \dot{m}_v h_v - \dot{m}_{s,o} h_s \left(T_{htf,i}, p_v, x_o\right) \tag{26}$$

The limiting fluid is the heat transfer fluid if $\dot{Q}_{htf-1} < \dot{Q}_{htf-2}$ Otherwise, the limiting fluid is the solution.
When the limiting fluid is the HTF, the maximum vapor flow rate that can be absorbed by the solution film in cooling mode $\dot{m}^{max}_{abs-cool}$ can be calculated by solving a set of five equations: equations (20)-(24), equation (22) being replaced by equation (27):

$$\dot{m}_{s,i} h_{s,i} - \dot{m}_{s,o} h_{s,o} + \dot{m}_v h_v = \dot{m}_{htf} Cp_{htf} \left(T_{s,o-ad} - T_{htf,i}\right) \tag{27}$$

Figure 8 shows the maximum vapor flow rate that can be absorbed by the solution for an infinitely long absorber as a function of the solution Reynolds number and the HTF flow rate in nominal conditions ($T_{s,i} = T_{htf,i} = 30$ °C, $x_i = 60\%$wt; $p_v = 1000$ Pa). The amount of vapor that can be absorbed by the solution increases as the HTF flow rate increases (increase of the cooling capacity). The maximum absorption rate varies linearly with the solution Reynolds number in adiabatic and isothermal mode. It is controlled by the HTF flow rate in cooling mode when the limiting fluid is the heat transfer fluid. In this case, the maximum absorption rate increases with the solution Reynolds number.

4.2.2. HTF Inlet temperature effects

In the experiments presented, the absorber cooling is not very efficient, due to the low heat transfer coefficient between the absorber and the heat transfer fluid. For example, for the nominal conditions (see Table 3) the thermal resistance between the heat transfer fluid and the absorber wall ($R_{htf} = \dfrac{1}{\alpha_{htf-w}} = 0.00083$ K m^2 W^{-1}) is the main limitation to the overall heat transfer. The thermal resistance in the wall and between the wall and the film

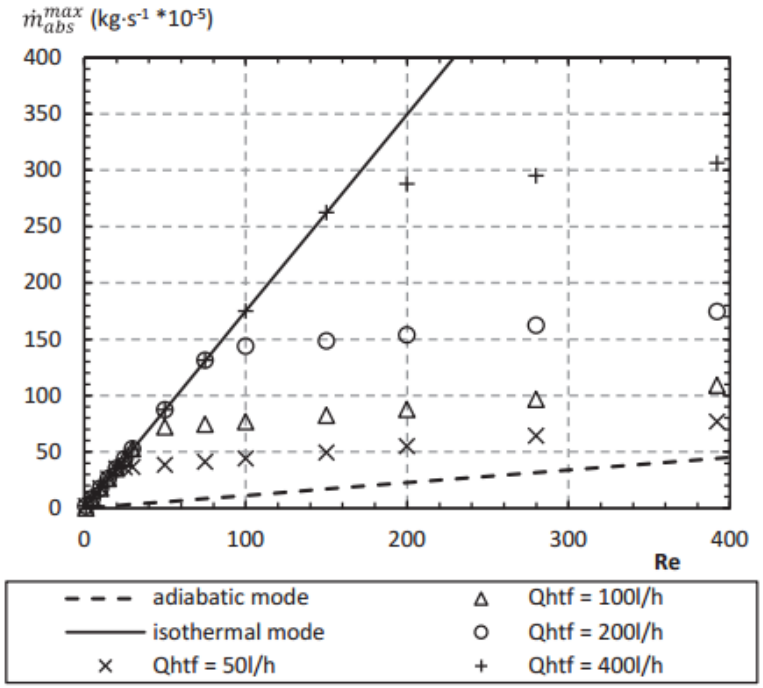

Figure 8: Maximum vapor absorption flow rate as a function of the Reynolds number in nominal conditions (Table 3) for different cooling conditions.

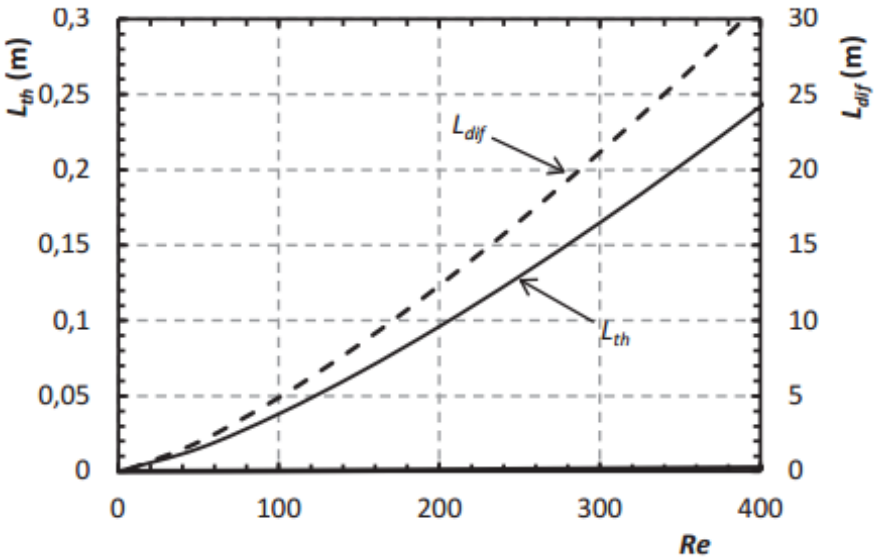

Figure 9: Establishment length of the thermal and diffusive boundary layer in the LiBr solution falling film, for nominal conditions (Table 3).

are, respectively, $R_w = \frac{e_w}{\lambda_w} = 0.00019\ \mathrm{K\,m^2\,W^{-1}}$ and $R_{film} = \frac{1}{\alpha_{film-w}} = 0.00075\ \mathrm{K\,m^2\,W^{-1}}$. This is especially caused by the low heat transfer fluid flow rate (chosen to obtain accurate values of the heat evacuated by this fluid), and the nonoptimal internal channel geometry. Therefore, to increase the cooling effect, an inlet cooling temperature ($\mathrm{T}_{i,htf}$) lower than the solution inlet temperature was imposed. Different inlet cooling temperatures were tested on the 220-mm-long absorber plate.

Figure 7a and b presents the absorption rate as a function of the solution Reynolds number and the inlet HTF temperature (presented as a subcooling temperature difference: $\Delta T_{cool} = T_{s,i} - T_{htf,i}$, with $T_{s,i} = 30$ °C). $\dot{m}^{max}_{abs-iso}$ for the isothermal condition as a function of the inlet Reynolds number is plotted with a dotted line in Figure 7a.

Contrary to the adiabatic condition, the solution is never at equilibrium with vapor at the end of the exchanger. The degree of deviation from equilibrium of the solution with the vapor is very high and leads to a higher absorption rate compared to the adiabatic condition.

As observed in previous numerical and experimental studies [7, 14, 15], Figure 7b shows that the absorption rate increases quasi-linearly as the HTF inlet temperature increases. A lower HTF temperature decreases the solution interface temperature and consequently increases the deviation from equilibrium and then the absorption rate.

However, the lower the flow rate of the falling film, the more significant the impact of increasing the subcooling (i.e., increasing ΔT) is. For low Reynolds numbers ($30 \leq \mathrm{Re} \leq 50$ in Figure 7b), the absorption rate increase is about 150% for a subcooling temperature increases of 20 °C. The absorption rate increase falls to 70% for a Reynolds number around 130. Moreover, for Reynolds numbers higher than 180, the subcooling temperature has no significant impact on the absorption rate for this absorber.

Two effects play an important role in this phenomenon: the increase of the film's thermal resistance, which increases as the film thickness increases, and the increase of the entry length (the length for which the thermal boundary layer that develops from the interface reaches the plate; see Figure 9), which increases as the Reynolds number rises. Note that in the cooled falling film configuration, the interface of the falling film is affected by the cooling effect of the plate only when the thermal boundary layer that develops from the plate reaches the interface of the film. Therefore, the greater the flow rate and the longer the entry length, the less the length is affected by the cooling effect. These two effects limit the cooling of the solution interface, and therefore the absorption rate, when the solution flow rate increases.

Figure 9 shows the changes in the establishment length Lth of the thermal boundarylayerin the solution fallingfilm and for the nominal conditions. It is calculated using the following equation [25]:

$$\frac{L_{th}}{e} = \frac{17}{640} Re \cdot Pr \tag{28}$$

Figure 9 shows that, for the 220-mm-long exchanger plate, the HTF is no longer heated by the solution film as soon as the Reynolds number of the falling film exceeds 375. For a Reynolds number of 200, the thermal boundary layer establishment length is around of

100 mm. The effective film length whose interface is influenced by plate cooling is therefore about 120 mm. For the falling film Reynolds numbers (15e350) studied, the HTF flow of the experimental bench is not sufficient to adequately cool the LiBr solution (the temperature is imposed by the solution; case 'b' presented in section 4.2.1).
The entry length L_{dif} of the diffusion boundary layer in the solution falling film for the nominal conditions is calculated using equation (29) [25]:

$$\frac{L_{dif}}{e} = \frac{17}{640} Re \cdot Sc \tag{29}$$

In the range of Reynolds numbers studied, the diffusion entry length is about 100 times longer than the thermal entry length. This means that for a high efficient absorption process, the absorption rate is controlled by diffusive effects.

4.3. Equilibrium deviation effects

In an absorption process, the inlet driving force is defined as the difference between the solution equilibrium conditions at the inlet and the actual solution inlet conditions. It can be defined as a function of pressure ($\Delta p_{eq} = p_{eq}(T_{s,i}, x_i) - p_v$) or temperature ($\Delta T_{eq} = T_{eq}(p_v, x_i) - T_{s,i}$). Usually, the greater the inlet driving force, the greater the absorption rate is. Thus, any change in the inlet solution conditions results in a change in the driving force and then in the vapor absorption rate.
The effect of the solution inlet conditions (x_i , $T_{s,i}$) on the absorption rate is shown in Figure 10 for the adiabatic condition of the 220-mm exchanger. Experiments with different inlet solution temperatures (20-40 °C) and inlet solution mass fractions (57-60%wt) were conducted (the other test parameters were kept constant at the nominal values listed in Table 3). The overall results of these experiments are presented in Figure 10 using D T eq (the nominal conditions correspond to ΔT_{eq} = 17.5 °C). The equilibrium conditions are calculated using the LiBr solution properties defined in Ref. [24] and measurements of the absorber pressure and inlet temperature and mass fraction (see section 2.3).
The absorption rate increases linearly with the driving force. Moreover, the absorption rate increases from $5{\cdot}10^{-5}$ kg s^{-1} to $15{\cdot}10^{-5}$ kg s^{-1} when the inlet solution temperature changes from 40 °C to 20 °C (i.e.,ΔT_{eq} changes from 10 °C to 27.7 °C). Similarly, the absorption rate increases from $6{\cdot}10^{-5}$ kg s^{-1} to $10{\cdot}10^{-5}$ kg s^{-1} when the inlet LiBr mass fraction changes from 57%wt to 60%wt (i.e., ΔT_{eq} changes from 12 °C to 18.7 °C).

4.4. Absorber effectiveness

It is interesting to characterize the absorber performance using mass effectiveness (ϵ_m), which can be defined as the ratio between the actual absorption rate ($\dot{m}_{abs}$) and the maximum absorption rate ($\dot{m}_{abs}^{max}$) [5]:

$$\epsilon_m = \frac{\dot{m}_{abs}}{\dot{m}_{abs}^{max}} \tag{30}$$

The maximum absorption rate would be obtained in an infinitely long counter-flow absorber. It depends on the solution and HTF inlet conditions and can be calculated using the mass,

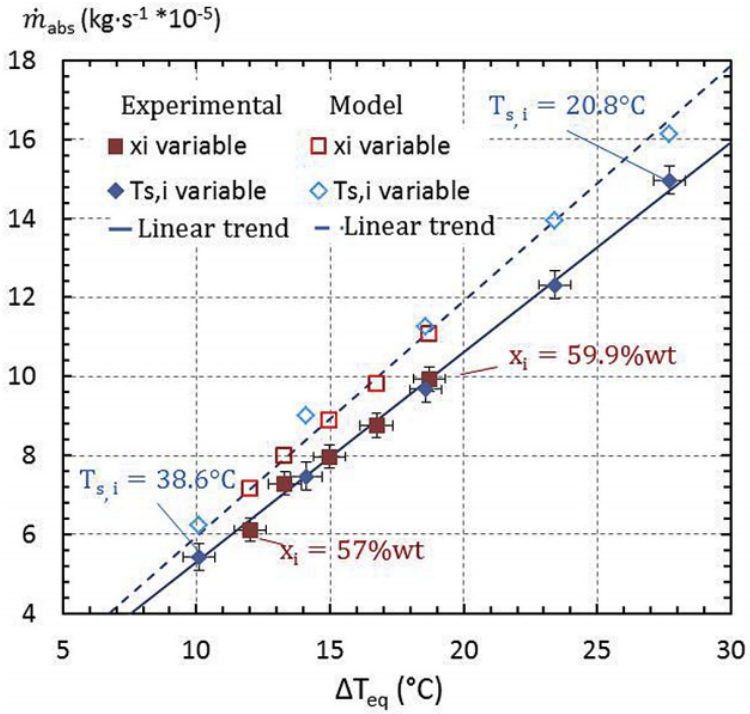

Figure 10: Experimental and numerical absorption rates as a function of the inlet driving force, for different inlet solution temperatures and mass fractions. Absorber length:220 mm.

species and energy balance equations of the absorber (as explained in section 4.1).
The exchanger effectiveness for the adiabatic and isothermal conditions and for two exchanger lengths (220 mm and 420 mm) are presented in Figure 11. The simulations were carried out for a Reynolds range of 0-300 and a driving force (ΔT_{eq}) range of 0-35 °C. The solution inlet conditions were set at the nominal conditions (see Table 3) and the vapor pressure was changed from 2635 Pa to 345 Pa (to change the driving force).

635 Pa to 345 Pa (to change the driving force). Figure11 shows that the effectiveness is greater in the adiabatic than in the isothermal mode. Indeed, in the first case the effectiveness ranges from 1 to 0.4, while it ranges from 0.54 to 0 in the second case. However, greater effectiveness in the adiabatic case does not correspond to a higher absorption rate since the maximum vapor mass flow rate that can be absorbed by the solution differs significantly between the two configurations (see Figure 8).
The very low effectiveness in the isothermal mode, especially for Reynolds numbers higher than 50, is caused by three different effects that limit absorption: the water mass diffusion within the solution liquid film, which is significantly smaller than the thermal diffusion (as explained in section 4.2); the warming of the solution, which affects equilibrium at the interface; and the heat transfer coefficient between the plate and the liquid film in the laminar regime, which decreases as the Reynolds number increases. As presented in Figure 9, the

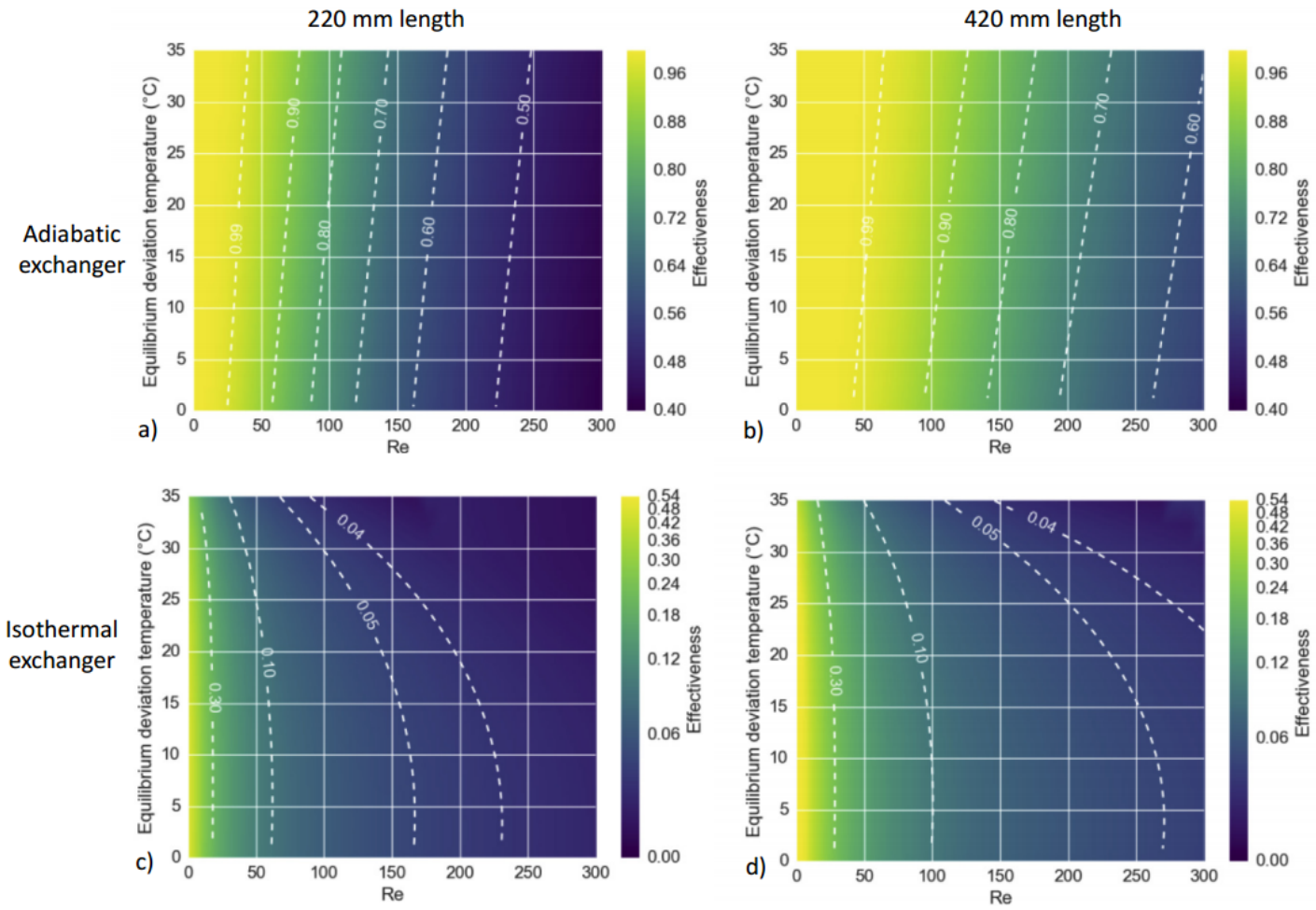

Figure 11: Absorber effectiveness as a function of the inlet equilibrium deviation factor and the inlet solution Reynolds number, a) for the adiabatic condition of the 220-mm absorber; b) for the adiabatic condition of the 420-mm absorber; c) for the isothermal condition of the 220-mm absorber; and d) for the isothermal condition of the 420-mm absorber.

exchanger length necessary for the falling film to perceive the cooling effect of the plate is around that of the exchanger length for the range of Reynolds numbers studied. For the geometries studied (220 mm and 420 mm long), the cooling impact is therefore limited and does not significantly increase the absorber performance.

Furthermore, Figure 11 shows that the effectiveness decreases as the Reynolds number decreases in both adiabatic and isothermal conditions. This phenomenon was highlighted in section 4.1 because of the increase in the entry lengths of the thermal boundary layers with the increasing Reynolds number. For the same absorber length, the higher the entry lengths, the lower the absorption rate and the lower the absorber effectiveness. In contrast, as shown in Figure 7, increasing the absorber length increases its absorption rate and therefore its

effectiveness.
Figure 11a and b shows that, in the adiabatic case, the driving force (equilibrium deviation temperature) has a low impact on effectiveness. In the range of driving force studied, the absorption rate evolves quasi-linearly with the driving force (see section 4.3). Therefore, at a constant Reynolds number, the effectiveness decreases slightly (less than 5%) with the driving force. This low level of change can be explained by the variation of the solution's thermophysical properties caused by the change of the equilibrium temperature (due to the change of the operating pressure).
For the isothermal case (Figure 11c and d), two different impacts of the driving force are observed. At low driving force ($\Delta T_{eq} < 15$ °C), the effectiveness evolves in a similar way to the adiabatic case. In contrast, for higher driving forces, a substantial decrease of the effectiveness can be observed as the driving force increases. This is partly due to the nonlinear evolution of the maximum absorption rate with the driving force, caused by the nonlinear evolution of the solution's equilibrium (due to the considerable variation of the solution's mass fraction along the absorber in the isothermal configuration with high driving forces), as can be seen in Figure 12.

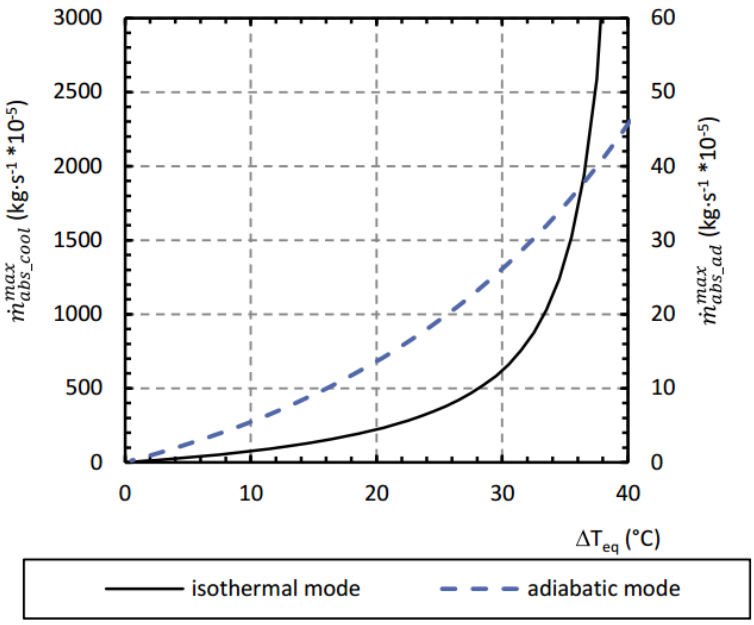

Figure 12: Maximum vapor absorption flow rate as a function of the driving force for adiabatic and isothermal thermal conditions.

5. Conclusion

This study investigates a plate-type falling film absorber. An innovative absorber design consisting in a vertical grooved falling film absorber designed to obtain good wettability of the absorber plate, even at low solution flow rates, leading to a laminar solution flow regime.

The knowledge of the absorption characteristics of this absorber is a key point for its sizing. Using experimental and numerical tools, the operation and the performance of this absorber were investigated for the water/LiBr working pair, through the quantity of vapor absorbed by the solution falling film (the mass absorption rate).
Absorption rate measurements were taken on large-scale absorbers (100 mm wide x 220/420 mm long). The impact of several design and operating conditions (absorber length, cooling water temperature, solution temperature, mass fraction, flow rate, etc.) were studied. Experimentally, a high absorption rate is achieved: as high as $7{\cdot}10^{-3}$ $\mathrm{kg\,s^{-1}\,m^{-2}}$. The strong influence of the solution flow rate and the driving force on the absorption rate was highlighted. In both cases, the absorption rate at least triples in the range of Reynolds numbers and driving force studied (i.e., 15-300 and driving force: 10-30 °C). Furthermore, the experimental results showed that the absorption rate increases linearly as the HTF inlet temperature decreases. The lower the falling film flow rate is, the greater this increase is.
A 1D stationary model developed to describe the water vapor absorption on a laminar vertical falling film exchanger was presented and validated. This model was used to characterize the absorber performance, using mass effectiveness, for a wide range of operating conditions. At identical operating conditions, greater effectiveness in the adiabatic mode than in the isothermal condition was highlighted. The low effectiveness of the isothermal case stems mainly from the absorber length studied being close to the length necessary for the falling film to perceive the cooling effect of the plate in the range of Reynolds numbers studied.
The next step is the design and the testing of a prototype of vertical grooved falling film absorber/desorber dedicated to a cooling machine (10 kW of cold production). The test of this prototype will allow demonstrating the feasibility of this absorber technology on a large scale.

Acknowledgements

We thank the DCNS for their financial support.

Bibliography

[1] A. Aliane, S. Abboudi, C. Seladji, B. Guendouz, An illustrated review on solar absorption cooling experimental studies, Renewable and Sustainable Energy Reviews 65 (2016) 443–458. doi:10.1016/j.rser.2016.07.012.
URL http://www.sciencedirect.com/science/article/pii/S1364032116303379

[2] J. Zhang, H.-H. Zhang, Y.-L. He, W.-Q. Tao, A comprehensive review on advances and applications of industrial heat pumps based on the practices in China, Applied Energy 178 (2016) 800–825. doi:10.1016/j.apenergy.2016.06.049.
URL http://www.sciencedirect.com/science/article/pii/S0306261916308248

[3] K. E. N'Tsoukpoe, H. Liu, N. Le Pierrès, L. Luo, A review on long-term sorption solar energy storage, Renewable and Sustainable Energy Reviews 13 (9) (2009) 2385–2396. doi:10.1016/j.rser.2009.05.008.
URL http://linkinghub.elsevier.com/retrieve/pii/S1364032109001129

[4] D. Aydin, S. P. Casey, S. Riffat, The latest advancements on thermochemical heat storage systems, Renewable and Sustainable Energy Reviews 41 (2015) 356–367. doi:10.1016/j.rser.2014.08.054.
URL http://www.sciencedirect.com/science/article/pii/S1364032114007308

[5] M. R. Islam, N. E. Wijeysundera, J. C. Ho, Heat and mass transfer effectiveness and correlations for counter-flow absorbers, International Journal of Heat and Mass Transfer 49 (21–22) (2006) 4171–4182. doi:10.1016/j.ijheatmasstransfer.2006.04.002.
URL http://www.sciencedirect.com/science/article/pii/S0017931006002328

[6] S. Bigham, D. Yu, D. Chugh, S. Moghaddam, Moving beyond the limits of mass transport in liquid absorbent microfilms through the implementation of surface-induced vortices, Energy 65 (2014) 621–630. doi:10.1016/j.energy.2013.11.068.
URL http://www.sciencedirect.com/science/article/pii/S0360544213010384

[7] M. Mortazavi, R. Nasr Isfahani, S. Bigham, S. Moghaddam, Absorption characteristics of falling film LiBr (lithium bromide) solution over a finned structure, Energy 87 (2015) 270–278. doi:10.1016/j.energy.2015.04.074.
URL http://www.sciencedirect.com/science/article/pii/S0360544215005290

[8] M. S. El-Genk, H. H. Saber, An Investigation of the Breakup of an Evaporating Liquid Film, Falling Down a Vertical, Uniformly Heated Wall, Journal of Heat Transfer 124 (1) (2001) 39–50. doi:10.1115/1.1420712.
URL http://dx.doi.org/10.1115/1.1420712

[9] K. E. N'Tsoukpoe, N. Le Pierrès, L. Luo, Experimentation of a LiBr–H2o absorption process for long-term solar thermal storage: Prototype design and first results, Energy 53 (2013) 179–198. doi:10.1016/j.energy.2013.02.023.
URL http://www.sciencedirect.com/science/article/pii/S0360544213001370

[10] B. Fumey, R. Weber, P. Gantenbein, X. Daguenet-Frick, S. Stoller, R. Fricker, V. Dorer, Operation Results of a Closed Sorption Heat Storage Prototype, Energy Procedia 73 (2015) 324–330. doi:10.1016/j.egypro.2015.07.698.
URL http://linkinghub.elsevier.com/retrieve/pii/S1876610215014666

[11] M. Raisul Islam, N. E. Wijeysundera, J. C. Ho, Performance study of a falling-film absorber with a film-inverting configuration, International Journal of Refrigeration 26 (8) (2003) 909–917. doi:10.1016/S0140-7007(03)00078-1.
URL http://www.sciencedirect.com/science/article/pii/S0140700703000781

[12] K. E. N'Tsoukpoe, N. Le Pierrès, L. Luo, Numerical dynamic simulation and analysis of a lithium bromide/water long-term solar heat storage system, Energy 37 (1) (2012) 346–358.
URL http://www.sciencedirect.com/science/article/pii/S0360544211007389

[13] D. Arzoz, P. Rodriguez, M. Izquierdo, Experimental study on the adiabatic absorption of water vapor into LiBr–H2o solutions, Applied Thermal Engineering 25 (5–6) (2005) 797–811. doi:10.1016/j.applthermaleng.2004.08.003.
URL http://www.sciencedirect.com/science/article/pii/S1359431104002388

[14] E. García-Rivera, J. Castro, J. Farnós, A. Oliva, Numerical and experimental investigation of a vertical LiBr falling film absorber considering wave regimes and in presence of mist flow, International Journal of Thermal Sciences 109 (2016) 342–361. doi:10.1016/j.ijthermalsci.2016.05.029.
URL http://www.sciencedirect.com/science/article/pii/S1290072916306767

[15] M. Medrano, M. Bourouis, A. Coronas, Absorption of water vapour in the falling film of water–lithium bromide inside a vertical tube at air-cooling thermal conditions, International Journal of Thermal Sciences 41 (9) (2002) 891–898. doi:10.1016/S1290-0729(02)01383-2.
URL http://www.sciencedirect.com/science/article/pii/S1290072902013832

[16] F. Babadi, B. Farhanieh, Characteristics of heat and mass transfer in vapor absorption of falling film flow on a horizontal tube, International Communications in Heat and Mass Transfer 32 (9) (2005) 1253–1265. doi:10.1016/j.icheatmasstransfer.2005.05.011.
URL http://www.sciencedirect.com/science/article/pii/S0735193305001119

[17] L. A. Domínguez-Inzunza, J. A. Hernández-Magallanes, P. Soto, C. Jiménez, G. Gutiérrez-Urueta, W. Rivera, Experimental assessment of an absorption cooling system utilizing a falling film absorber and generator, Applied Thermal Engineering 103 (2016) 1105–1111. doi:10.1016/j.applthermaleng.2016.05.014.

URL http://www.sciencedirect.com/science/article/pii/S1359431116306664
[18] D. S. Kim, C. A. Infante Ferreira, Solar refrigeration options – a state-of-the-art review, International Journal of Refrigeration 31 (1) (2008) 3–15. doi:10.1016/j.ijrefrig.2007.07.011.
URL http://www.sciencedirect.com/science/article/pii/S0140700707001478
[19] M. Flamensbeck, F. Summerer, P. Riesch, F. Ziegler, G. Alefeld, A cost effective absorption chiller with plate heat exchangers using water and hydroxides, Applied Thermal Engineering 18 (6) (1998) 413–425. doi:10.1016/S1359-4311(97)00049-5.
URL http://www.sciencedirect.com/science/article/pii/S1359431197000495
[20] J. D. Killion, S. Garimella, A critical review of models of coupled heat and mass transfer in falling-film absorption, International Journal of Refrigeration 24 (8) (2001) 755–797. doi:10.1016/S0140-7007(00)00086-4.
URL http://www.sciencedirect.com/science/article/pii/S0140700700000864
[21] D. Yu, J. Chung, S. Moghaddam, Parametric study of water vapor absorption into a constrained thin film of lithium bromide solution, International Journal of Heat and Mass Transfer 55 (21–22) (2012) 5687–5695. doi:10.1016/j.ijheatmasstransfer.2012.05.064.
URL http://www.sciencedirect.com/science/article/pii/S0017931012003857
[22] R. Nasr Isfahani, S. Moghaddam, Absorption characteristics of lithium bromide (LiBr) solution constrained by superhydrophobic nanofibrous structures, International Journal of Heat and Mass Transfer 63 (2013) 82–90. doi:10.1016/j.ijheatmasstransfer.2013.03.053.
URL http://www.sciencedirect.com/science/article/pii/S0017931013002603
[23] A. H. H. Ali, Design of a compact absorber with a hydrophobic membrane contactor at the liquid–vapor interface for lithium bromide–water absorption chillers, Applied Energy 87 (4) (2010) 1112–1121. doi:10.1016/j.apenergy.2009.05.018.
URL http://www.sciencedirect.com/science/article/pii/S0306261909002153
[24] J. Castaing-Lavignottes, Aspects thermodynamiques et technico-économiques des systèmes à absorption liquide, Tech. rep., CNAM, Laboratoire IFFI (2001).
URL https://encrypted.google.com/url?sa=t&rct=j&q=&esrc=s&source=web&cd=1&ved=0ahUKEwjPmJPb6bvNAhUMlxQKHW8mArQQFggbMAA&url=https%3A%2F%2Fwww.researchgate.net%2Ffile.PostFileLoader.html%3Fid%3D563bd4f55e9d97c8558b459e%26assetKey%3DAS%253A292553996947456%2540144676171713 6&usg=AFQjCNG4Ji_h8-ehcX7DJKwwLABtfX4-nw&sig2=yU7WXAuQghe1Smfsw8FaUA&bvm=bv.124817099,d.d24&cad=rja
[25] C. Flores, Etude des transferts de masse et de chaleur au sein d'un absorbeur eau/bromure de lithium, Ph.D. thesis, Université de Grenoble (2014).
URL http://hal.univ-savoie.fr/tel-01062936/
[26] R. Moffat, Contribution to the theory of single-sample uncertainty analysis, Journal of Fluid Engineering 104 (1982) 250–260.
[27] J.-K. Kim, C. W. Park, Y. T. Kang, The effect of micro-scale surface treatment on heat and mass transfer performance for a falling film H2o/LiBr absorber, International Journal of Refrigeration 26 (5) (2003) 575–585. doi:10.1016/S0140-7007(02)00147-0.
URL http://www.sciencedirect.com/science/article/pii/S0140700702001470
[28] F. Huaylla, N. Le Pierrès, B. Stutz, E. N'Tsoukpoe, Performance analysis of multifunctional exchangers implemented in an interseasonal sorption heat storage system, in: International Soprtion Heat Pump Conference (ISHPC), March 31 - April 3, Washington DC, USA, 2014.
[29] Z. Yuan, K. E. Herold, Thermodynamic Properties of Aqueous Lithium Bromide Using a Multiproperty Free Energy Correlation, HVAC&R Research 11 (3) (2005) 377–393. doi:10.1080/10789669.2005.10391144.
URL http://www.tandfonline.com/doi/abs/10.1080/10789669.2005.10391144
[30] N. Brauner, Non-isothermal vapour absorption into falling film, International Journal of Heat and Mass Transfer 34 (3) (1991) 767–784. doi:10.1016/0017-9310(91)90124-W.
URL http://www.sciencedirect.com/science/article/pii/001793109190124W
[31] G. Grossman, Simultaneous heat and mass transfer in film absorption under laminar flow, International

Journal of Heat and Mass Transfer 26 (3) (1983) 357–371. doi:10.1016/0017-9310(83)90040-6. URL http://www.sciencedirect.com/science/article/pii/0017931083900406

[32] V. P. Carey, Liquid Vapor Phase Change Phenomena: An Introduction to the Thermophysics of Vaporization and Condensation Processes in Heat Transfer Equipment, Second Edition, 2nd Edition, CRC Press, New York, 2007.

[33] F. P. Incropera, Fundamentals of Heat and Mass Transfer, John Wiley & Sons, 2011.

[34] S. Karami, B. Farhanieh, A numerical study on the absorption of water vapor into a film of aqueous LiBr falling along a vertical plate, Heat and Mass Transfer 46 (2) (2009) 197–207, wOS:000273102300007. doi:10.1007/s00231-009-0557-y.

Annex

All the experimental results presented in this paper are detailed in the following tables:

Table .4: Experimental results of the 220-mm absorber length for different solution flow rates in the cooled condition, with $\Delta T = T_{s,i} - T_{htf,i} = 0$°C.

$\Delta T_{cool} = T_{s,i} - T_{htf,i}$	$\dot{m}_{s,i}$ (kg/h)	Re		x_i (%wt)	x_o (%wt)	p_v (Pa)	$T_{s,i}$ °C	$T_{s,o}$ °C	$T_{htf,i}$ °C	$\dot{m}_{htf,i}$ (kg/h)	$\dot{m}_{abs} \cdot 10^5$ (kg/s)		$\dot{m}_{abs} \cdot 10^3$ (kg s^{-1} m^{-2})	
0	65.86	181	±2	60.44	60.24	991.29	30.22	38.04	30.06	86.49	13.5	±1.8	6.1	±0.8
0	83.95	233	±2.6	60.26	60.12	1002.89	30.01	36.33	29.61	52.70	13.5	±1.4	6.1	±0.6
0	117.17	335	±3.7	60.00	59.93	998.61	30.55	35.98	29.86	52.18	15.68	±1.6	7.1	±0.7
0	48.63	129	±1.4	60.63	60.35	999.42	29.33	37.38	29.56	53.24	11.1	±1.2	5.0	±0.5
0	41.58	111	±1.2	60.59	60.27	997.42	29.41	37.93	29.87	65.90	10.3	±1.4	4.7	±0.6
0	14.48	39	±0.4	60.61	60.09	1000.10	29.92	35.38	30.27	31.99	4.15	±0.7	1.9	±0.3

Table .5: Experimental results of the 220-mm absorber length for different solution flow rates in the cooled condition, with $\Delta T = T_{s,i} - T_{htf,i} = 5$°C.

$\Delta T_{cool} = T_{s,i} - T_{htf,i}$	$\dot{m}_{s,i}$ (kg/h)	Re		x_i (%wt)	x_o (%wt)	p_v (Pa)	$T_{s,i}$ °C	$T_{s,o}$ °C	$T_{htf,i}$ °C	$\dot{m}_{htf,i}$ (kg/h)	$\dot{m}_{abs} \cdot 10^5$ (kg/s)		$\dot{m}_{abs} \cdot 10^3$ (kg s^{-1} m^{-2})	
5	46.74	126	±1.4	60.56	60.27	1010.65	29.78	37.36	25.62	28.10	11.61	±0.85	5.3	±0.4
5	40.22	110	±1.2	60.34	59.99	998.69	29.63	37.10	25.52	27.74	10.43	±0.8	4.7	±0.4
5	74.59	207	±2.3	60.29	60.12	1000.41	30.23	36.76	25.53	27.92	14.1	±1	6.4	±0.5
5	127.32	352	±3.9	60.44	60.38	1003.51	30.45	34.97	25.50	27.85	16	±1.4	7.3	±0.6

Table .6: Experimental results of the 220-mm absorber length for different solution flow rates in the cooled condition, with $\Delta T = T_{s,i} - T_{htf,i} = 10$°C.

$\Delta T_{cool} = T_{s,i} - T_{htf,i}$	$\dot{m}_{s,i}$ (kg/h)	Re		x_i (%wt)	x_o (%wt)	p_v (Pa)	$T_{s,i}$ °C	$T_{s,o}$ °C	$T_{htf,i}$ °C	$\dot{m}_{htf,i}$ (kg/h)	$\dot{m}_{abs} \cdot 10^5$ (kg/s)		$\dot{m}_{abs} \cdot 10^3$ (kg s^{-1} m^{-2})	
10	48.06	131	±1.5	60.49	60.12	1001.87	30.15	36.18	21.46	32.24	12.7	±1	5.8	±0.5
10	67.65	189	±2.1	60.24	60.09	1002.42	30.37	35.41	21.50	32.06	13.29	±1.1	6.0	±0.5
10	119.67	341	±3.8	60.04	60.04	1001.17	30.62	33.67	21.53	32.20	13.60	±1.5	6.2	±0.7
10	18.28	50	±0.6	60.39	59.73	995.27	30.17	28.84	21.36	32.48	5.41	±0.8	2.5	±0.4
10	35.79	100	±1.1	60.20	59.85	1001.22	30.05	36.36	21.30	32.64	11.62	±0.9	5.3	±0.4

Table .7: Experimental results of the 220-mm absorber length for different solution flow rates in the cooled condition, with $\Delta T = T_{s,i} - T_{htf,i} = 20°C$.

$\Delta T_{cool} =$ $T_{s,i} - T_{htf,i}$	$\dot{m}_{s,i}$ (kg/h)	Re		x_i (%wt)	x_o (%wt)	p_v (Pa)	$T_{s,i}$ °C	$T_{s,o}$ °C	$T_{htf,i}$ °C	$\dot{m}_{htf,i}$ (kg/h)	$\dot{m}_{abs} \cdot 10^5$ (kg/s)		$\dot{m}_{abs} \cdot 10^3$ (kg s^{-1} m^{-2})	
20	18.81	50	±0.6	60.58	59.88	1005.44	29.52	27.11	10.78	32.92	9.91	±0.97	4.5	±0.4
20	71.26	196	±2.2	60.35	60.22	1000.62	30.10	32.73	10.79	32.37	14.4	±1.3	6.5	±0.6
20	98.89	276	±3.0	60.27	60.22	1000.21	30.31	32.73	10.83	31.86	15.6	±1.5	7.1	±0.7
20	125.48	349	±3.9	60.33	60.32	1000.15	30.45	32.27	10.84	31.96	15.6	±1.7	7.1	±0.8
20	34.06	90	±1.0	60.72	60.36	976.82	29.48	31.40	12.32	33.91	13	±1.1	5.9	±0.5

Table .8: Experimental results of the 220-mm absorber length for different solution flow rates, in the adiabatic condition.

$\Delta T_{cool} =$ $T_{s,i} - T_{htf,i}$	$\dot{m}_{s,i}$ (kg/h)	Re		x_i (%wt)	x_o (%wt)	p_v (Pa)	$T_{s,i}$ °C	$T_{s,o}$ °C	$T_{htf,i}$ °C	$\dot{m}_{htf,i}$ (kg/h)	$\dot{m}_{abs} \cdot 10^5$ (kg/s)		$\dot{m}_{abs} \cdot 10^3$ (kg s^{-1} m^{-2})	
-	47.45	132	±1.5	60.19	59.97	997.84	29.82	38.79	-	-	9.68	±0.32	4.4	±0.1
-	5.99	15	±0.2	60.69	60.09	999.61	28.26	44.07	-	-	2.14	±0.04	1.0	±0.1
-	26.68	73	±0.8	60.33	60.02	999.32	29.42	40.77	-	-	6.88	±0.18	3.1	±0.1
-	68.03	187	±2.1	60.42	60.27	1001.92	30.30	38.41	-	-	12.56	±0.46	5.7	±0.2
-	108.80	300	±3.3	60.62	60.55	999.37	30.94	36.74	-	-	14.58	±0.75	6.6	±0.3

Table .9: Experimental results of the 220-mm absorber length for different inlet solution temperatures, in the adiabatic condition.

$\Delta T_{cool} =$ $T_{s,i} - T_{htf,i}$	$\dot{m}_{s,i}$ (kg/h)	Re		x_i (%wt)	x_o (%wt)	p_v (Pa)	$T_{s,i}$ °C	$T_{s,o}$ °C	$T_{htf,i}$ °C	$\dot{m}_{htf,i}$ (kg/h)	$\dot{m}_{abs} \cdot 10^5$ (kg/s)		$\dot{m}_{abs} \cdot 10^3$ (kg s^{-1} m^{-2})	
-	51.93	114	±1.3	60.45	60.13	1007.06	20.81	33.45	-	-	14.96	±0.35	6.8	±0.2
-	51.26	124	±1.4	60.52	60.24	1002.46	25.16	35.70	-	-	12.31	±0.35	5.6	±0.2
-	52.91	160	±1.7	60.37	60.20	1003.24	34.17	40.36	-	-	7.47	±0.36	3.4	±0.2
-	47.83	156	±1.7	60.63	60.47	1000.01	38.65	43.63	-	-	5.43	±0.33	2.5	±0.2
-	49.72	135	±1.5	60.42	60.22	999.34	29.73	38.26	-	-	9.67	±0.34	4.4	±0.2

Table .10: Experimental results of the 220-mm absorber length for different inlet solution mass fractions, in the adiabatic condition.

$\Delta T_{cool} =$ $T_{s,i} - T_{htf,i}$	$\dot{m}_{s,i}$ (kg/h)	Re		x_i (%wt)	x_o (%wt)	p_v (Pa)	$T_{s,i}$ °C	$T_{s,o}$ °C	$T_{htf,i}$ °C	$\dot{m}_{htf,i}$ (kg/h)	$\dot{m}_{abs} \cdot 10^5$ (kg/s)		$\dot{m}_{abs} \cdot 10^3$ (kg s^{-1} m^{-2})	
-	45.94	130	±1.4	59.87	59.65	1080.21	29.86	39.50	-	-	9.94	±0.31	4.5	±0.1
-	44.90	130	±1.4	59.56	59.38	995.05	29.84	38.38	-	-	8.75	±0.30	4.0	±0.1
-	44.19	137	±1.5	58.59	58.43	999.97	29.76	37.63	-	-	7.96	±0.30	3.6	±0.1
-	43.72	144	±1.5	57.74	57.61	1000.52	29.72	36.98	-	-	7.28	±0.30	3.3	±0.1
-	42.05	145	±1.5	57.06	56.95	1000.42	29.66	35.98	-	-	6.12	±0.29	2.8	±0.1

Table .11: Experimental results of the 420-mm absorber length for different solution flow rate, in the adiabatic condition.

$\Delta T_{cool} =$ $T_{s,i} - T_{htf,i}$	$\dot{m}_{s,i}$ (kg/h)	Re		x_i (%wt)	x_o (%wt)	p_v (Pa)	$T_{s,i}$ °C	$T_{s,o}$ °C	$T_{htf,i}$ °C	$\dot{m}_{htf,i}$ (kg/h)	$\dot{m}_{abs} \cdot 10^5$ (kg/s)		$\dot{m}_{abs} \cdot 10^3$ (kg s^{-1} m^{-2})	
-	48.33	126	±1.4	60.88	60.52	995.32	29.50	41.25	-	-	12.87	±0.33	3.1	±0.1
-	42.77	119	±1.3	60.05	59.74	1005.12	29.57	40.94	-	-	11.05	±0.25	2.6	±0.1
-	12.95	34	±0.4	60.99	60.38	1035.89	29.57	42.38	-	-	3.74	±0.09	0.9	±0.02
-	28.91	77	±0.9	60.58	60.19	995.39	29.30	42.48	-	-	8.63	±0.19	2.1	±0.05
-	66.71	189	±2.1	59.95	59.73	970.45	29.98	39.43	-	-	14.34	±0.45	3.4	±0.1
-	105.71	292	±3.2	60.50	60.37	1003.00	30.58	38.50	-	-	19.02	±0.71	4.5	±0.2